

# Coupled Wing-Propeller Aerodynamic Optimization Using the Adjoint Method

Heyecan U. Koyuncuoglu\* and Ping He<sup>†</sup>  
*Iowa State University, Ames, Iowa, 50011, USA*

**Increasing attention to urban air mobility with electric propulsion causes an increased interest in propeller aircraft design and optimization.** Various studies have been focusing on optimizing the aerodynamic performance of wings and propellers. However, existing aerodynamic optimization studies optimized the wing and propeller separately. In this study, we develop the capability to simultaneously optimize the wing and propeller. We use a high-fidelity computational fluid dynamics solver to simulate the wing aerodynamics, and the propeller is modelled by adding an actuator disk in the flow field. We develop a smoothed actuator disk formulation that allows us to change the location and radius of the propeller during the optimization, along with the wing shape. We use the discrete adjoint approach to compute the derivatives and couple it with a gradient-based optimization framework. The above adjoint-based optimization framework can use a large number of design variables to allow a large design freedom for both wing and propeller. We perform a total of nine aerodynamic optimizations with various propeller parameters as the design variables. We also consider optimization with single and double propeller configurations. We observe that the spanwise location and the outer radius are the two most important parameters for the propeller, and using more propeller parameters as the design variables generally result in larger wing drag reduction. For example, optimizing the wing shape while allowing the actuator location and outer radius to move results in more than 20% wing drag reduction, compared with the baseline design. This study serves as the starting point for more detailed high-fidelity wing-propeller aerodynamic optimizations.

## I. Introduction

THE history of flight begins with propeller aircraft that used combustion engines. Even though there are new types of propulsion systems, propeller systems are still preferred for aircraft flying at low speeds, such as Light Sport Aircraft, Trainer Aircraft, Floatplanes, Amphibian Aircraft, etc. With all that, increasing research interest in electric propulsion systems led to an increase in research of design and optimization of propeller aircraft [1–10]. Electric propulsion systems have many benefits like low emission, low maintenance cost, using less complex engines compared to combustion engines, and more importantly allowing distributed propulsion [1]. Aircraft weights and sizes can be reduced by using distributed propulsion systems. For example, NASA's X-57 aircraft is optimized from a Tecnam P2006T as baseline. The wing of X-57 is 58% smaller than the baseline design and the lift coefficient of that wing is nearly 3 times of baseline design [10].

There have been many studies focusing on design and optimization of wing and propeller systems [3–17]. Kroo [11] investigated the interaction of wing and propeller and found that the optimal lift distribution on wing with a propeller is not elliptical like a single wing. Witkowski et al. [12] performed both experiments and computational fluid dynamics (CFD) analysis to investigate the time-averaged performance of a wing with a tractor propeller. They used semiempirical and vortex lattice methods for CFD applications. Both their experiments and CFD analysis of a wing with a tractor propeller configuration showed that increasing propeller power decreases wing-induced drag and increases propeller efficiency and lift-curve slope. Gomariz-Sancha et al. [13] performed CFD analysis by using steady Reynolds-Averaged Navier-Stokes (RANS) method with actuator disk and unsteady RANS with full propeller blade model. They showed that actuator disk can also adequately represent propeller effects on the airframe with less computational cost. Stokkermans et al. [14] also showed that RANS method with Spalart-Allmaras turbulence can be used to model aerodynamic interactions between a wing and a tractor propeller located at the wingtip. Also, they showed that actuator disk model reduced the computational cost with only a small penalty on the lift distribution on

\*PhD Student, Department of Aerospace Engineering, AIAA Member.

<sup>†</sup>Assistant Professor, Department of Aerospace Engineering, AIAA Senior Member.

the wing and steady flow field. Deere et al. [10] performed both CFD analysis by using FUN3D, STAR-CCM+, and OVERFLOW software and experiments to investigate the effects of distributed propulsion with tractor propellers. They used both actuator disk approach (in FUN3D, STAR-CCM+) and rotating propellers (OVERFLOW), the CFD analysis agreed well with the experiment for the X-57 wing. Alba et al. [15] developed a surrogate-based multi-disciplinary design optimization (MDO) framework for wing optimization by considering effects of tractor propellers on the wing aerodynamic characteristics. The planform and airfoil shape parameters were used as the design variables. Their MDO model consists of coupled wing-propeller aerodynamic model, which uses isolated propeller and isolated wing models, structural model (wing weight) and performance model. Hwang and Ning [4] performed MDO analysis on the X-57 model. They used aerodynamics, propulsion, and structure models by using blade element momentum theory, vortex lattice theory, and finite element analysis. They also considered mission profile parameters as design variables. Moore and Ning [6] extended this study by investigating effects of distributed propulsion on the takeoff performance for urban aircraft. Stokkermans et al. [16] investigated effects of auxiliary lateral propellers on helicopters. They used Airbus RACER helicopter, which has box-wing structures with pusher propellers, as their model. They found that the rotational flowfield at the wingtip increases propulsive efficiency of propellers. Chauhan and Martins [17] used RANS method to optimize a coupled wing and propeller, which is modeled as an actuator disk. They found out that the difference between optimizing the coupled wing and propeller and optimizing the wing itself then placing the propeller at the same location is small.

The previous studies mentioned above either isolated the wing and propeller and optimized them separately or used a fixed propeller and just optimized the wing. In this study, taking a step forward in this direction is aimed by optimizing the wing and propeller simultaneously with a high number of design variables. A tractor propeller is modeled by using actuator disk method, by that way steady CFD simulations were performed without modelling the detailed propellers. In addition, the actuator disk force is smoothed to allow continuous changes during the optimization. The longitudinal, lateral and vertical locations and the outer radius of the propeller are considered as the design variables for the propeller. The wing geometry is embedded in a free form deformation (FFD) box, which is then manipulated by 120 FFD control points. The wing cross-sectional shape and twist is controlled by these points by mapping of locations change of these points to the wing surface. Coupled wing and propeller models with single and double propellers are investigated. Also, we use the adjoint approach to efficiently compute the gradient for a large number of design variables.

The rest of the paper is organized as the following three sections. In Section II, the mathematical background of steady-state flow simulation is explained, then the discrete adjoint derivative computation methodology is described, and finally the high-fidelity optimization framework is briefly explained. In Section III, the CFD setup is validated using experimental results, then the adjoint derivative calculation is verified, and optimizations of single wing model, a wing and a propeller model, and a wing and two propellers model are presented. In Section IV, the findings of this study is concluded.

## II. Method

In this section, we elaborate on the high-fidelity CFD simulation process, followed by the discrete adjoint approach for gradient computation.

### A. Steady-State Turbulent Flow Simulation

The primal flow analysis is conducted by using OpenFOAM's rhoSimpleFoam solver with modifications that improve the convergence. rhoSimpleFoam solves 3D, steady-state turbulent flows governed by the compressible Navier-Stokes (NS) equations;

$$\nabla \cdot \rho \mathbf{U} = 0 \quad (1)$$

$$\nabla \cdot (\rho \mathbf{U} \mathbf{U}) + \nabla p - \nabla \cdot \mu_{\text{eff}} (\nabla \mathbf{U} + \nabla \mathbf{U}^T) - \mathbf{S}_U = 0 \quad (2)$$

$$\nabla \cdot (\rho e \mathbf{U}) + \nabla \cdot (0.5 \rho |\mathbf{U}|^2 + p \mathbf{U}) - \alpha_{\text{eff}} \nabla \cdot (\nabla e) - S_e = 0 \quad (3)$$

where  $\mathbf{U} = [u, v, w]$  is velocity the vector,  $p$  is the pressure,  $\rho$  is the density,  $\mu_{\text{eff}} = \mu + \mu_t$  is the effective viscosity, i.e., the sum of dynamic viscosity and turbulent eddy viscosity,  $e$  is the internal energy,  $\alpha_{\text{eff}}$  is the effective thermal diffusivity, and  $\mathbf{S}_U$  and  $S_e$  are the actuator source terms to mimic the added force and energy in the flow field, respectively. We will elaborated on the computation of these source terms in Sec. III.

The Spalart-Allmaras model is used to connect the turbulent eddy viscosity to the mean flow variables, the details of this formulation and description of the terms can be found on their paper [18]:

$$\nabla \cdot (\mathbf{U} \tilde{v}) + \frac{1}{\sigma} \{ \nabla \cdot [(v + \tilde{v}) \nabla \tilde{v}] + C_{b1} |\nabla \tilde{v}|^2 \} - C_{b1} \tilde{S} \tilde{v} + C_{w1} f_w \left( \frac{\tilde{v}}{d} \right)^2 = 0 \quad (4)$$

Then, the semi-implicit method for pressure-linked equations (SIMPLE) [19] algorithm, originally proposed for incompressible flow, is extended to solve the compressible NS equations. After discretization of momentum equation (2), an intermediate velocity field is solved using the pressure field from the previous iteration of initial guess,  $p^0$ .

$$a_P \mathbf{U}_P + \sum_N a_N \mathbf{U}_N = -\nabla p^0 - \mathbf{S}_U \quad (5)$$

where  $a$  is the finite-volume discretization coefficient, subscript  $P$  and  $N$  denote respectively the control volume cell and all neighboring cells. Rearranging the above equation, we get:

$$a_P \mathbf{U}_P = - \sum_N a_N \mathbf{U}_N - \mathbf{S}_U - \nabla p^0 = \mathbf{H} - \nabla p^0 \quad (6)$$

where  $\mathbf{H}$  represents the influence of all neighboring velocities:

$$\mathbf{H} = - \sum_N a_N \mathbf{U}_N - \mathbf{S}_U \quad (7)$$

The face flux,  $\phi$  is introduced to linearize the convective term:

$$\int_S \rho \mathbf{U} \mathbf{U} \cdot d\mathbf{S} = \sum_f \mathbf{U}_f [\rho \mathbf{U}_f \cdot \mathbf{S}_f] = \sum_f \phi^0 \mathbf{U}_f \quad (8)$$

where the subscript  $f$  denotes the cell face. At first iteration  $\phi$  can be obtained from the previous iteration or an initial guess.

Intermediate velocity field is obtained by solving the discretized momentum equation (6). The next step is satisfying the continuity equation. The new pressure field is computed by using a pressure Poisson equation which is constructed by coupling the continuity equation with the momentum equation. The discretized continuity equation is:

$$\int_S \rho \mathbf{U} \cdot d\mathbf{S} = \sum_f [\rho \mathbf{U}]_f \cdot \mathbf{S}_f = 0 \quad (9)$$

$\mathbf{U}_f$  is computed by interpolating the cell-centered velocity  $\mathbf{U}_P$ , which is obtained from Eq. 6, onto the cell face:

$$[\rho \mathbf{U}]_f = \left( \frac{\rho \mathbf{H}}{a_p} \right)_f - \left( \frac{\rho}{a_p} \right)_f (\nabla p)_f \quad (10)$$

This momentum interpolation method is effective in mitigating the oscillating pressure issue, as proposed by [20]. The Poisson equation is obtained by substituting Eq. 10 into Eq. 9:

$$\nabla \cdot \left( \frac{\rho}{a_p} \nabla p^1 \right) = \nabla \cdot \left( \frac{\rho \mathbf{H}}{a_p} \right) \quad (11)$$

The updated pressure field,  $p^1$ , is used to update the face flux and the velocity field;

$$\phi^1 = [\rho \mathbf{U}]_f \cdot \mathbf{S}_f = \left[ \left( \frac{\rho \mathbf{H}}{a_p} \right)_f - \left( \frac{\rho}{a_p} \right)_f (\nabla p^1)_f \right] \cdot \mathbf{S}_f \quad (12)$$

$$\mathbf{U}^1 = \left( \frac{1}{a_p} \right) [\mathbf{H} - \nabla p^1] \quad (13)$$

The above steps make the velocity and pressure fields satisfy both continuity and momentum equations. After this, the density is updated using the new pressure and compressibility variable ( $\psi = 1/RT$ ):

$$\rho = p\psi \quad (14)$$

Next, the energy equation (3) is solved to obtain the new internal energy  $e$ . Then, a Newton-Raphson method is used to solve the compressibility  $\psi$  based on the internal energy  $e$ . Finally, an updated turbulence viscosity,  $\nu_t$ , is obtained by solving Eq. (3). The above steps will be repeated until all the governing equations converge.

Note that the built-in rhoSimpleFoam solver may diverge when solving general compressible flow for aerospace engineering problems. We have implemented the bounding for all flow variables to improve the robustness of the solver. To be more specific, we prescribe upper and lower bounds for pressure, velocity, density, internal energy, and turbulent variables right after their values are updated.

## B. Discrete Adjoint Derivative Computation

We use the discrete adjoint method to compute the derivatives for optimization. The function of interest is the function of both the design and state variables:

$$f = f(\mathbf{x}, \mathbf{w}) \quad (15)$$

where  $\mathbf{x} \in \mathbb{R}^{n_x}$  is the design vector, and  $\mathbf{w}^n \in \mathbb{R}^{n_w}$  is flow state variable vector. The chain rule is applied to obtain the  $df/d\mathbf{x}$ :

$$\left[ \frac{df}{d\mathbf{x}} \right]_{1 \times n_x} = \left[ \frac{\partial f}{\partial \mathbf{x}} \right]_{1 \times n_x} + \left[ \frac{\partial f}{\partial \mathbf{w}} \right]_{1 \times N_w} \left[ \frac{d\mathbf{w}}{d\mathbf{x}} \right]_{N_w \times n_x} \quad (16)$$

The partial derivatives in Eq. (16) are relatively cheap to evaluate because they only involve explicit computations. However, the total derivative  $d\mathbf{w}/d\mathbf{x}$  is expensive because both terms are determined implicitly. Similarly, the chain rule is applied to flow residual vector,  $\mathbf{R} \in \mathbb{R}^{n_w}$ , to solve the  $d\mathbf{w}/d\mathbf{x}$ . Because of the governing equations are independent of the values of design variables  $\mathbf{x}$ , the total derivative  $d\mathbf{R}/d\mathbf{x}$  must be zero:

$$\frac{d\mathbf{R}}{d\mathbf{x}} = \frac{\partial \mathbf{R}}{\partial \mathbf{x}} + \frac{\partial \mathbf{R}}{\partial \mathbf{w}} \frac{d\mathbf{w}}{d\mathbf{x}} = 0 \quad (17)$$

Substituting Eq. (16) into Eq. (15):

$$\left[ \frac{df}{d\mathbf{x}} \right]_{1 \times n_x} = \left[ \frac{\partial f}{\partial \mathbf{x}} \right]_{1 \times n_x} - \left[ \frac{\partial f}{\partial \mathbf{w}} \right]_{1 \times N_w} \left[ \frac{\partial \mathbf{R}}{\partial \mathbf{w}} \right]_{N_w \times N_w}^{-1} \left[ \frac{d\mathbf{R}}{d\mathbf{x}} \right]_{N_w \times n_x} = \left[ \frac{\partial f}{\partial \mathbf{x}} \right]_{1 \times n_x} - [\boldsymbol{\psi}^T]_{N_w \times 1} \left[ \frac{d\mathbf{R}}{d\mathbf{x}} \right]_{N_w \times n_x} \quad (18)$$

where  $\boldsymbol{\psi}$  is the adjoint vector. Transposing the Jacobian and solve with  $[df/d\mathbf{w}]^T$  as the right-hand side yields the adjoint equations:

$$\left[ \frac{\partial \mathbf{R}}{\partial \mathbf{w}} \right]_{N_w \times N_w}^T \cdot [\boldsymbol{\psi}]_{N_w \times 1} = \left[ \frac{\partial f}{\partial \mathbf{w}} \right]_{N_w \times 1} \quad (19)$$

Substituting Eq. (19) into Eq. (16):

$$\frac{df}{d\mathbf{x}} = \frac{\partial f}{\partial \mathbf{x}} - \boldsymbol{\psi}^T \frac{\partial \mathbf{R}}{\partial \mathbf{x}} \quad (20)$$

Since the design variable is not explicitly present in Eq. (19), the adjoint equations are needed to solve only once for each function of interest. Therefore, its computational cost is independent of the number of design variables, but proportional to the number of objective functions. This approach is also known as the adjoint method and it is advantageous for aerodynamic design, because typically there are only a few functions of interest but several hundred design variables can be used.

In this study, the discrete adjoint derivative computation is based on an open-source, object-oriented adjoint framework DAFoam [21, 22]. DAFoam uses a Jacobian-free adjoint approach, in which the partial derivatives and matrix-vector products are computed using the automatic differentiation, as detailed in Kenway et al. [23].

We use the generalized minimal residual (GMRES) iterative linear equation solver in the PETSc [24] library to solve the adjoint equation. A nested preconditioning strategy with the additive Schwartz method is used as the

global preconditioner and the incomplete lower and upper (ILU) factorization approach with zero fill-in for the local preconditioning. The preconditioner matrix  $[\partial \mathbf{R} / \partial \mathbf{w}]_{RC}^T$  is constructed by approximating the residuals and their linearizations [21] to improve convergence. The construction of  $[\partial \mathbf{R} / \partial \mathbf{w}]_{RC}^T$  is only done for the first time instance and then is reused for the adjoint equation. This treatment significantly reduces the adjoint runtime because the constructing  $[\partial \mathbf{R} / \partial \mathbf{w}]_{RC}^T$  consists of about 30% of the adjoint runtime.

### C. High-fidelity aerodynamic optimization framework (MACH-Aero)

The open-source MACH-Aero framework [25] is used to perform high-fidelity aerodynamic optimization in this study. MACH-Aero consists of six major modules: pre-processing, geometry parametrization, volume mesh deformation, flow simulation, adjoint computation, and optimizer. Each module interacts with input and output parameters. In the pre-processing module, the volume mesh of baseline geometry is generated by using OpenFOAM's built-in mesh generation tool "snappyHexMesh", and a Python script is used to generate the free-form deformation (FFD) control points. Sparse nonlinear optimizer (SNOPT) optimization package of "pyOptSparse" [26] is used as the optimizer to update the design variables in this study. The updated design variables are then used for the geometry parametrization by "pyGeo" [27], which calculates design surface deformation, geometric constraints, and their derivatives. IDWarp [28] uses an inverse-distance weighted approach to update volume mesh by using output of the "pyGeo" and the updated volume mesh from the pre-processing module. High-fidelity CFD tool "OpenFOAM" is used as the flow solver to compute the state variables, physical fields, objective functions, and constraint functions by using the updated volume mesh. "DAFoam" is then used as adjoint solver to compute the derivatives of objective and constraint functions with respect to the design variables [22]. After that, the optimizer "pyOptSparse" uses the objective and constraint functions and their derivatives to compute updated design variables, and send them to the "pyGeo" module. This loop continues till convergence criteria satisfied.

## III. Results and Discussion

In this section, firstly the coupled wing propeller model is validated by using experimental data from Veldhuis [29]. Then, Jacobian-free adjoint derivative computation's accuracy is verified by comparing with the forward-mode automatic differentiation method. After that, nine different optimizations cases by using 3 different optimization setups are performed, as shown in Table 1. The main objective of this paper is to investigate how effective are design variables and their combinations on the drag coefficient. The other actuator design parameters, such as thrust and advance ratio, are out of scope of this study and will be considered in future works.

### A. Validation of the wing-propeller CFD model

The propeller wing interference model (PROWIM), which is used by Veldhuis [29] in their experimental study, is used to create the baseline model to validate our CFD solver. The chord of this wing is 0.24 m and the half wingspan of

**Table 1 Summary of the 9 optimization cases with different number of propellers. All cases use the same shape and twist variables for the wing but different variations of propeller design variables. All cases use the wing drag as the objective function.**

Name	Number of Actuators	Actuator Design Variables
Wing_Only	0	-
Wing_Propeller_Fixed	1	-
Wing_Propeller_x	1	$x$
Wing_Propeller_y	1	$y$
Wing_Propeller_z	1	$z$
Wing_Propeller_xyz	1	$x, y, z$
Wing_Propeller_xydr2	1	$x, y, z, r_2$
Wing_2Propellers_Fixed	2	-
Wing_2Propellers_zr2	2	$z, r_2$

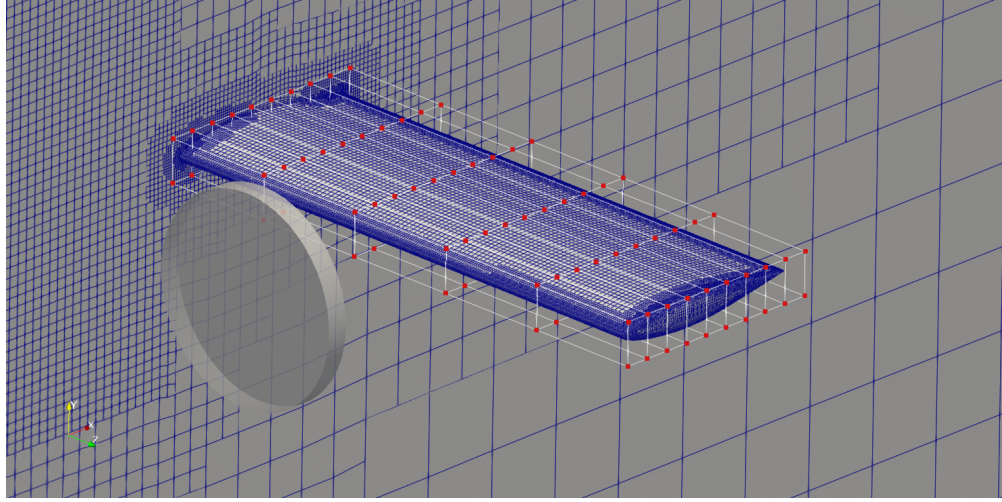


**Fig. 1 Verification model features; 690,000 cells mesh, FFD box with 120 control points and initial position of actuator**

it is 0.64 m. The incidence angle of wing is 4 degree. Unlike the wing geometry, the propeller is not an exact 3D model of Veldhuis [29], instead of that it is modeled as an actuator disk. Inner radius of this actuator is 0.035 m and the outer radius is 0.12 m. The rotation direction of propeller is inboard-up. The flow condition is compressible with Reynolds number  $2.2 \times 10^5$ , the flow velocity is 49.5 m/s, the temperature is 300 K, the pressure is 101.325 kPa, and the total axial force generated by the propeller is 38.9N. Four unstructured mesh with different number of cells are generated to investigate mesh convergence by using snappyHexMesh package and the computational domain extends 50 chords in each direction from the leading edge of the wing at symmetry plane. The flow convergence tolerance of the solver is  $10^{-8}$ . Spalart Allmaras turbulence model is used with  $\tilde{\nu} = 5.5 \times 10^{-5}$  at the far field. Figure 1 shows the mesh with 690,000 cells of the wing, the free form deformation (FFD) box and the position of the actuator disk. The disk is placed to show the actuator, where the axial and tangential force are applied initially.

All analyses and optimizations are run on the Skylake cores of the Nova cluster of ISU. The Skylake nodes are equipped with Intel Skylake 6140 Xeon CPUs running at 2.3 GHz, where each node has 36 CPU cores and 384 GB of memory [30].

We use the radial distribution functions, proposed by Hoekstra [31], to calculate the axial force and tangential forces of the actuator disk. However, directly using these functions can cause discontinuities and numerical instability when moving the propeller during optimizations. To overcome this problem, a smoothed actuator disk model, similar to what we proposed in [32], is applied to remove this discontinuities in the radial and streamwise directions. The axial force ( $x$  direction) equation without smoothing is:

$$f_x(\hat{r}) = \hat{F} \hat{r}^m \left( \frac{a - \hat{r}}{a} \right)^n \quad (21)$$

where the parameters  $m = 1.0$ ,  $n = 0.2$  and  $a = 1.0$  are used as suggested by Hoekstra [31],  $\hat{F}$  is the scaling factor to ensure that the integral actuator source over the entire flow domain equals the targeted axial force.  $\hat{r}$  is the normalized radial location, which is defined as:

$$\hat{r} = \frac{r - r_1}{r_2 - r_1} \quad (22)$$

where  $r$  is the radial location,  $r_1$  is the inner radius of the actuator, and  $r_2$  is the outer radius radius of the actuator. The Gaussian smooth function is used to smooth the force distributions in axial and radial directions to eliminate the discontinuity. The modified axial force with smoothing is:

$$f_x(\hat{r}) = \begin{cases} \hat{F} \hat{r}_{min}^m \left( \frac{a - \hat{r}_{min}}{a} \right)^n e^{-(\Delta \hat{r}/\beta)^2} e^{-(\Delta x/\varepsilon)^2}, & \text{if } \hat{r} \leq \hat{r}_{min} \\ \hat{F} \hat{r}^m \left( \frac{a - \hat{r}}{a} \right)^n e^{-(\Delta x/\varepsilon)^2}, & \text{if } \hat{r}_{min} < \hat{r} < \hat{r}_{max} \\ \hat{F} \hat{r}_{max}^m \left( \frac{a - \hat{r}_{max}}{a} \right)^n e^{-(\Delta \hat{r}/\beta)^2} e^{-(\Delta x/\varepsilon)^2}, & \text{if } \hat{r} \geq \hat{r}_{max} \end{cases} \quad (23)$$

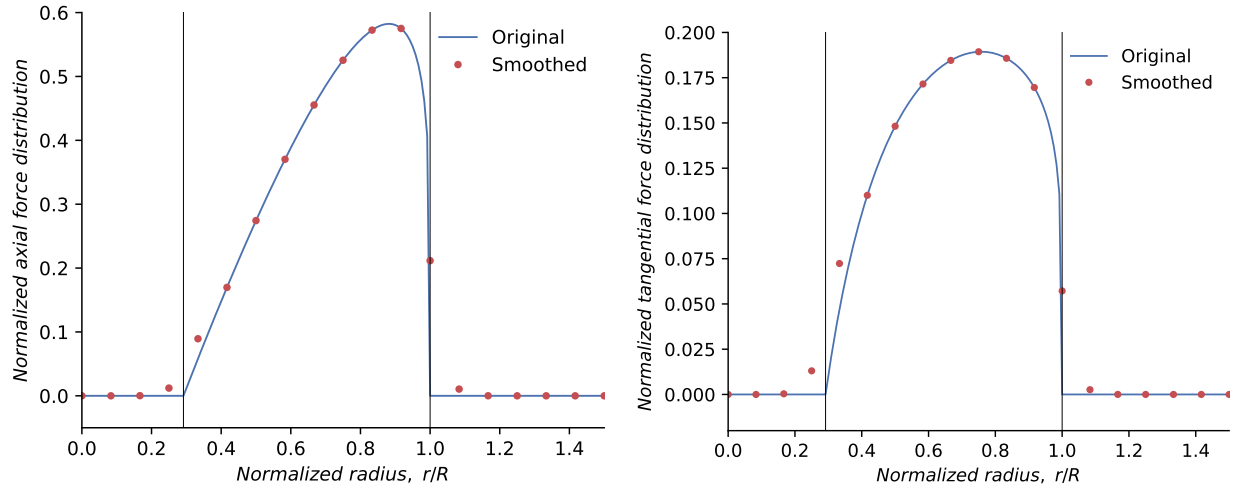


**Fig. 2** Distribution of unscaled axial force (left) and unscaled tangential force (right) on the normalized actuator radius.  $\varepsilon = 0.01$  is used to plot the smoothed force distributions.

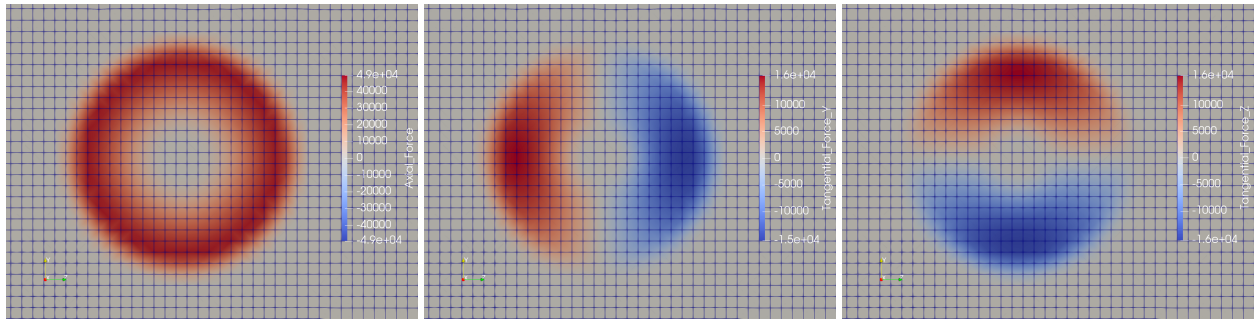


**Fig. 3** Contours of the scaled axial force (top), the scaled tangential force in  $y$  direction (bottom left) and the scaled tangential force in  $z$  direction (bottom right) at the center of the actuator and normal to the streamwise direction.

where  $\beta = \frac{\varepsilon}{r_2 - r_1}$  is the smoothness control parameter,  $\varepsilon$  is the mesh cell size in the actuator region,  $\hat{r}_{min} = \beta$  and  $\hat{r}_{max} = 1 - \beta$  are the starting and ending radial locations of smoothness function application, respectively,  $\Delta\hat{r}$  is the distance between  $\hat{r}$  and  $\hat{r}_{min}$  (if  $\hat{r} < \hat{r}_{min}$ ) or  $\hat{r}_{max}$  (if  $\hat{r} > \hat{r}_{max}$ ), and  $\Delta x$  is the streamwise distance between the cell center and the actuator center.

The tangential force is calculated by using smoothed tangential force equation:

$$f_\theta(\hat{r}) = f_x(\hat{r}) \frac{J}{\pi \left( \frac{r}{r_2} + 0.01 \left( 1 - \frac{r_1}{r_2} \right) \beta \right)} \quad (24)$$

where  $J = 0.85$  is the advance ratio. Here the second term in the denominator prevents the tangential force from going to infinity when  $r = 0$ .

The axial force and tangential force distributions without scaling with  $\hat{F}$  scaling factor on the normalized actuator radius can be seen on Fig. 2. Our smoothed distributions are in good agreement with the method suggested by Hoekstra [31]. At the regions around the inner and outer radius, the difference caused by smoothing are easily distinguishable. The contours of scaled axial and tangential forces can be seen on Fig. 3. As can be seen forces are continuously distributed and not cut at the inner and outer radius.

The summary of these 4 cases can be seen on Table 2. Even though both the  $C_D$  and  $C_L$  converges with increasing number of mesh cells, the  $C_L$  deviates from the experimental  $C_L$  [29].  $C_P$  distribution at 35% span and 62% span are computed and to compare with the digitally extracted data from the experimental data [29]. CFD results in agreement with the experimental data as can be seen on Fig.4 and Fig.5. Our results are also consistent with the results of Chauhan

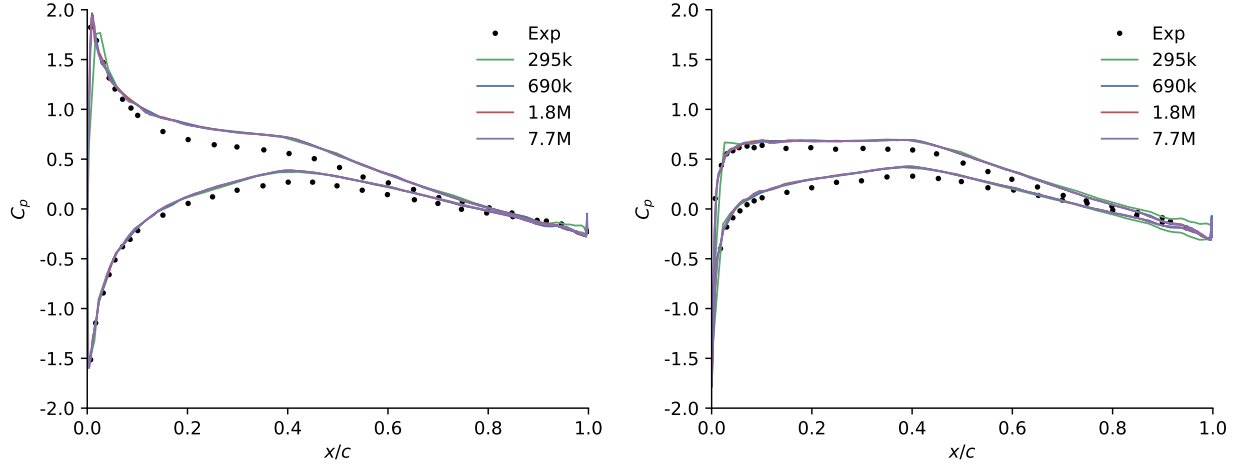


**Fig. 4** Comparison of  $C_P$  distribution with experimental data [29]. Left: 35% span. Right: 62% span

**Table 2** Mesh convergence (experimental data  $C_L=0.3276$ , digitally extracted from Veldhuis [29]). %  $\Delta C_D$  is the percentage decrease of  $C_D$  compared one coarser mesh, %  $C_L$  Error is the percentage difference between experimental and CFD results.

# of cells	$C_D$	% $\Delta C_D$	$C_L$	% $C_L$ Error
295,000	0.02873	—	0.32082	2.068
690,000	0.02505	14.651	0.31054	5.208
1,800,000	0.02393	4.710	0.30838	5.865
4,100,000	0.02359	1.435	0.30526	6.818
7,700,000	0.02331	1.180	0.30550	6.747

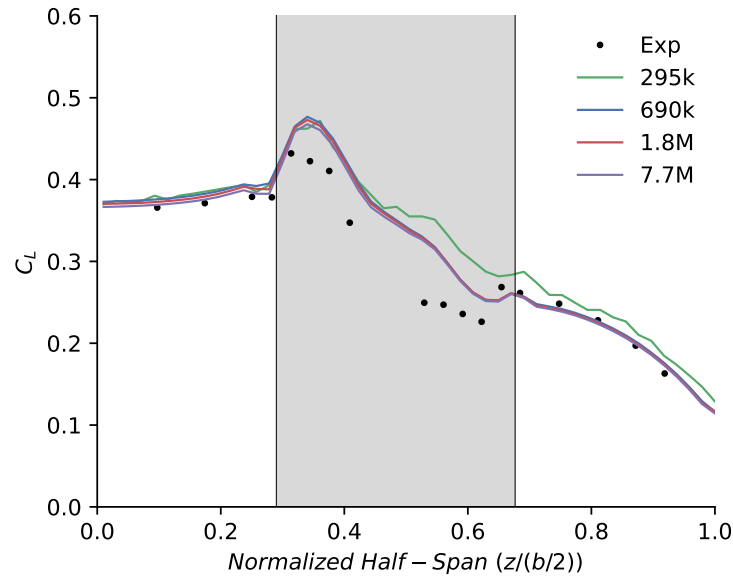


**Fig. 5** Comparison of  $C_L$  distribution on wing with experimental data [29]. Gray colored region is directly behind the actuator.

and Martins [17], who used a different flow and adjoint solver, and a structured mesh.

The aerodynamic parameters summarized in Table 2 are visualized in Fig.6. It is clear that both  $C_D$  and  $C_L$  converge,

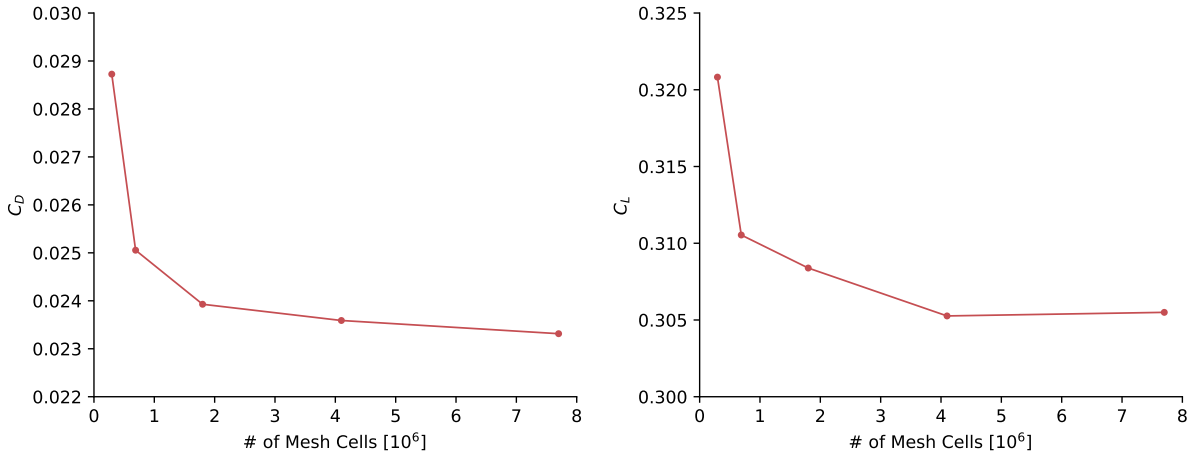


**Fig. 6** Change of aerodynamic parameters with the number of mesh cells. **Left:**  $C_D$ . **Right:**  $C_L$

this verifies the CFD model. However, there is an important point to be noted. The digitally extracted experimental data from Veldhuis [29] are not consistent. The experimental  $C_L$  value is higher than CFD solutions, however experimental  $C_L$  distribution is lower than them. This could be caused by different measurement methods used to collect data of  $C_L$  and  $C_D$  distribution. By considering this situation and the computational budget limit, the 690,000 cells unstructured mesh is used as optimization baseline setup.

### B. Verification of adjoint derivative accuracy

The adjoint derivative computation accuracy is evaluated by comparing adjoint derivatives calculated by using Jacobian Free method with reference adjoint derivatives calculated by using forward mode automatic differentiation

**Table 3** Comparison between the  $C_D$  adjoint derivatives and reference values computed by brute-force forward AD. Here  $a$  is the actuator variable ( $x$ ,  $y$ , and  $z$  are the space coordinates,  $r_2$  is the diameter of the actuator),  $\gamma$  is the twist with the subscript denoting different spanwise locations, and  $dy$  is the FFD point displacement with the subscript denoting the point index.

Variable	Reference	Adjoint	% Error
$a_x$	0.003315842	0.003315903	0.001840
$a_y$	0.006207284	0.006206252	0.016626
$a_z$	-0.004107091	-0.004107938	0.020623
$a_{r2}$	-0.014349480	-0.014349418	0.000432
$\gamma_0$	0.000896714	0.000896717	0.000335
$\gamma_1$	0.001338802	0.001338809	0.000523
$\gamma_2$	0.001543971	0.001543977	0.000389
$\gamma_3$	0.001508231	0.001508224	0.000464
$\gamma_4$	0.001213545	0.001213541	0.000330
$\gamma_5$	0.000505732	0.000505733	0.000198
$dy_{17}$	0.004270339	0.004270545	0.004824
$dy_{24}$	0.003074326	0.003074379	0.001724
$dy_{68}$	0.036909137	0.036909131	0.000016
$dy_{86}$	0.106581723	0.106582117	0.000370
$dy_{104}$	0.046141885	0.046142344	0.000995

**Table 4 Comparison between the  $C_L$  adjoint derivatives and reference values computed by brute-force forward AD.** Here  $a$  is the actuator variable ( $x$ ,  $y$ , and  $z$  are the space coordinates,  $r_2$  is the diameter of the actuator),  $\gamma$  is the twist with the subscript denoting different spanwise locations, and  $dy$  is the FFD point displacement with the subscript denoting the point index.

Variable	Reference	Adjoint	% Error
$a_x$	-0.007219892	-0.007220318	0.005900
$a_y$	0.015815276	0.015822219	0.043901
$a_z$	-0.001435260	-0.001429463	0.403899
$a_{r2}$	-0.075178420	-0.075179276	0.001139
$\gamma_0$	0.010063278	0.010063256	0.000219
$\gamma_1$	0.014568396	0.014568324	0.000494
$\gamma_2$	0.015928111	0.015927943	0.001055
$\gamma_3$	0.014790327	0.014790015	0.002109
$\gamma_4$	0.011030449	0.011030224	0.002040
$\gamma_5$	0.004029049	0.004029025	0.000596
$dy_{17}$	0.074168910	0.074168013	0.001209
$dy_{24}$	0.213647999	0.213647583	0.000195
$dy_{68}$	0.491416029	0.491416658	0.000128
$dy_{86}$	1.407708017	1.407708518	0.000036
$dy_{104}$	0.663670577	0.663673818	0.000488

(Forward-Mode AD). The wing surface embedded in the control points of FFD box and the change of locations of FFD points are transferred to the wing surface by mapping, and this process provides control over twist and wing cross-sectional shape. The verification of the drag and lift coefficient with respect to 15 of these FFD design variables, the actuator variables, and the twist variables and 5 randomly selected geometry variables, can be seen on Tables 3 and 4. The agreement of adjoint derivatives with reference values are generally 5 digits and the average relative error is less 0.001%, there are a few derivatives in agreement with just 4 digits, but their relative error are still less than 0.1%. The accuracy of adjoint derivatives are sufficient to use for numerical optimization.

**Table 5 Wing\_Only optimization problem formulation**

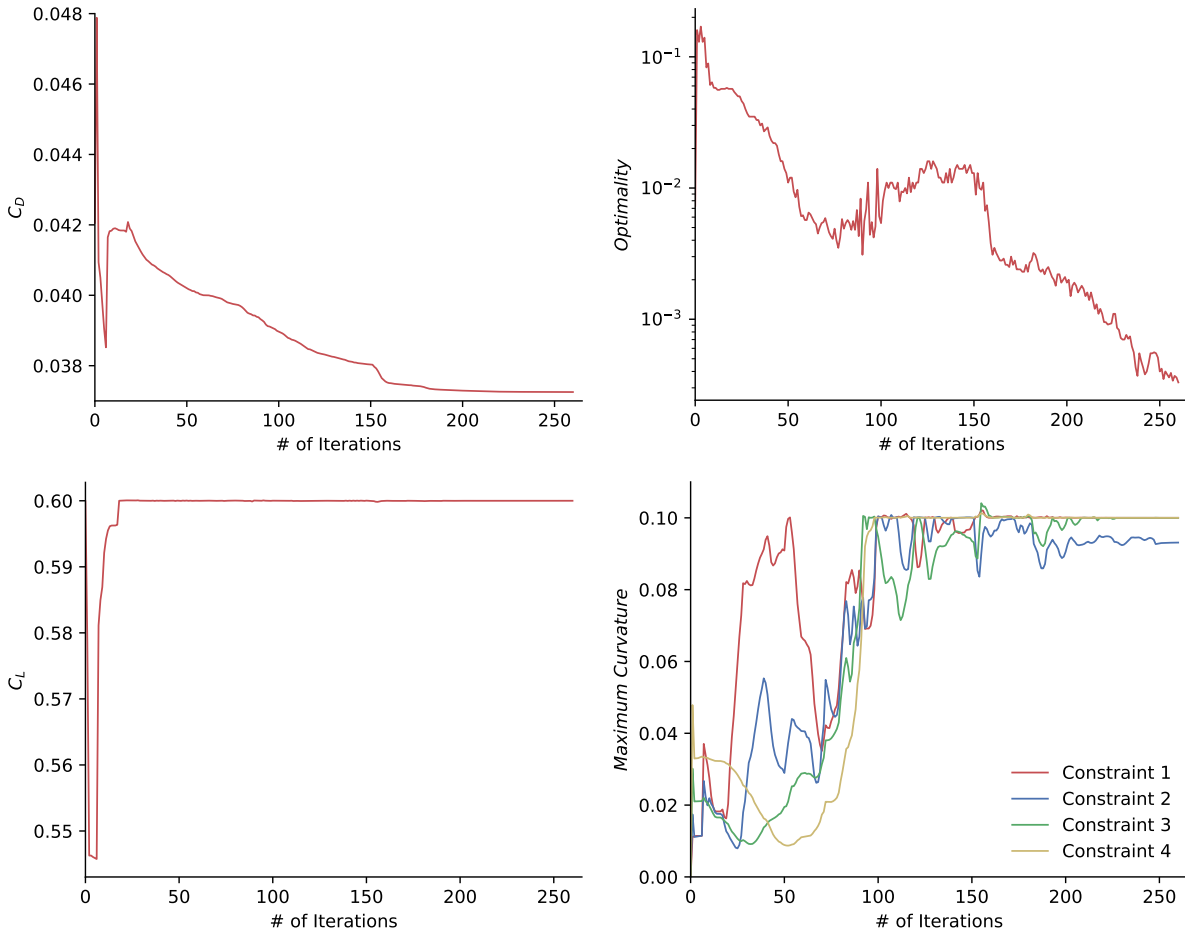
	Function/Variable	Description	Quantity
Minimize	$C_D$	Drag coefficient of the wing	
with respect to	$-10 \leq \gamma \leq 10$	Twist of each FFD section	6
	$-1.0 \leq \Delta y \leq 1.0$	Vertical displacements of FFD points	120
		<b>Total Design Variables</b>	<b>126</b>
subject to	$V_{bl} \leq V \leq 3 \cdot V_{bl}$	Minimum volume constraint	1
	$0.5 \cdot t_{bl} \leq t \leq 3 \cdot t_{bl}$	Minimum thickness constraint	240
	$\Delta y_{LE, \text{upper}} = \Delta y_{LE, \text{lower}}$	Fixed leading edge constraint	6
	$\Delta y_{TE, \text{upper}} = \Delta y_{TE, \text{lower}}$	Fixed trailing edge constraint	6
	$C_L = 0.6$	Lift constraint	1
	$r_{LE, bl} \leq r_{LE} \leq 3 \cdot r_{LE, bl}$	Leading edge radius constraint	1
	$0 \leq \kappa \leq 0.1$	Curvature constraints	4
		<b>Total Constraint Functions</b>	<b>259</b>

**Table 6 Summary of results for the Wing\_Only optimization**

	Baseline Design	Optimized Design	Change %
$C_D$	0.04206	0.03725	-11.4
$C_L$	0.5999	0.6000	-
Optimality	7.3E-03	3.3E-04	-
Feasibility	6.6E-06	1.4E-08	-

**C. Wing aerodynamic optimization without a propeller (Wing\_Only)**

In this section, results for aerodynamic shape optimization of the wing without a propeller is demonstrated. The optimization configuration is summarized in Table 5. The flow condition is compressible with Reynolds number  $2.2 \times 10^5$ , the flow velocity is 100 m/s with a Mach number 0.3, the temperature is 300 K and the pressure is 101.325 kPa. The objective function is the drag coefficient ( $C_D$ ) and nominal flight condition is at lift coefficient ( $C_L$ ) of 0.6, following Chauhan and Martins [17]. The design variables are the twist angle ( $\gamma$ ) and 120 FFD points moving in the vertical ( $y$ ) direction. The twist angle is changed by pitching the airfoil with respect to its quarter chord compared to changing the direction of free stream velocity typically used in steady-flow optimization. This strategy ensures the free stream is parallel to the wakes at longitudinal direction. 240 sampling points over the wing are used to control the airfoil thickness, which are bounded between half and three times of baseline thickness. 12 linear constraints are used to fix the

**Fig. 7 Convergence of optimization parameters and constraints. Top left:  $C_D$  is minimized. Top right: optimality is minimized. Bottom left:  $C_L$  is fixed as 0.6. Bottom right: curvature constraints bounded between 0.0 and 0.1**

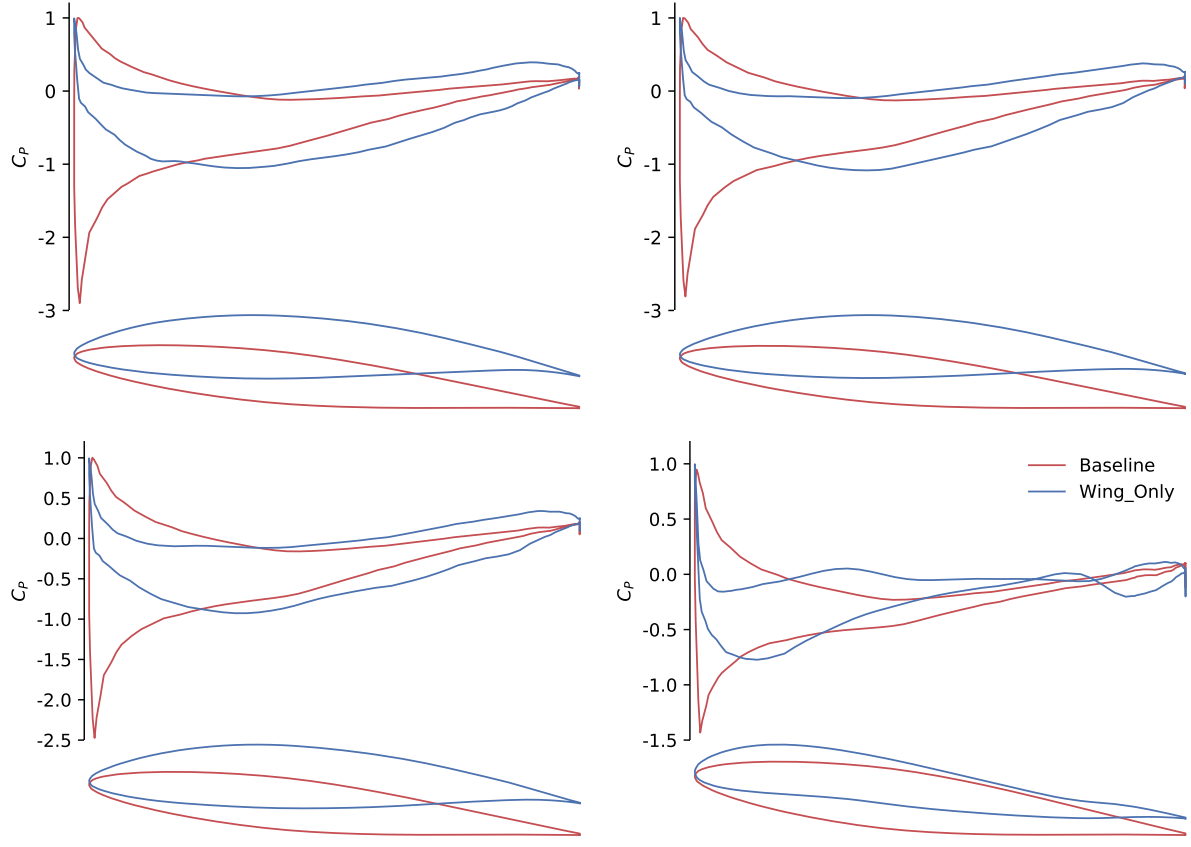


**Fig. 8** Change of  $C_P$  distribution and airfoil shape at different wing sections. Top left: 3% span. Top right: 31% span. Bottom left: 63% span. Bottom right: 94% span. Red color denotes baseline geometry, blue color denotes optimized geometry.

upper and lower surfaces of the leading and the trailing edges. A total volume constraint is bounded between one and three times of baseline volume. The lift coefficient is constrained to be equal to 0.6. The leading edge radius constraint bounds radius of the leading edge (2% of the chord is used) between one and three times of baseline radius.

The last constraint is the curvature constraint, which limits the spanwise curvature along the wing to prevent wavy geometries. In our previous work, we have imposed 2D curvature constraints to prevent wavy design surface during the optimization [21, 33]. However, the 2D curvature constraint doesn't not apply to the current study, because it will

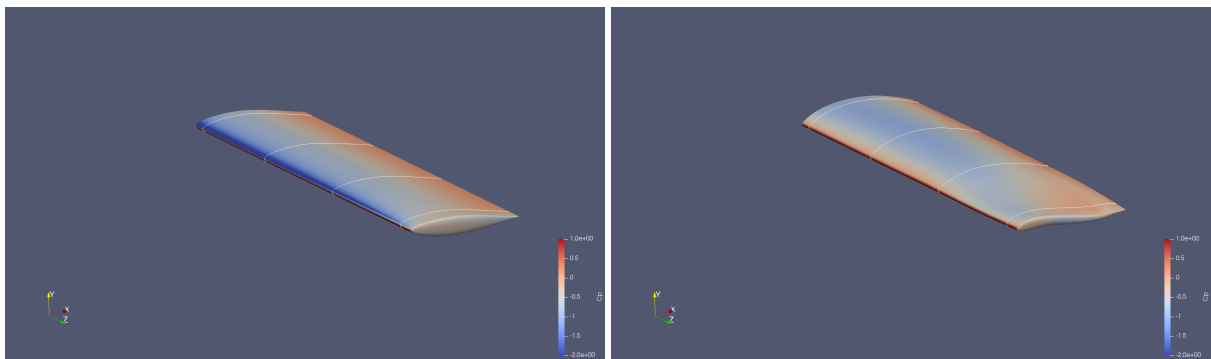


**Fig. 9** Baseline (left) and optimized (right) configurations. Also 4 wing sections used to show the change of  $C_P$  distribution are visible.

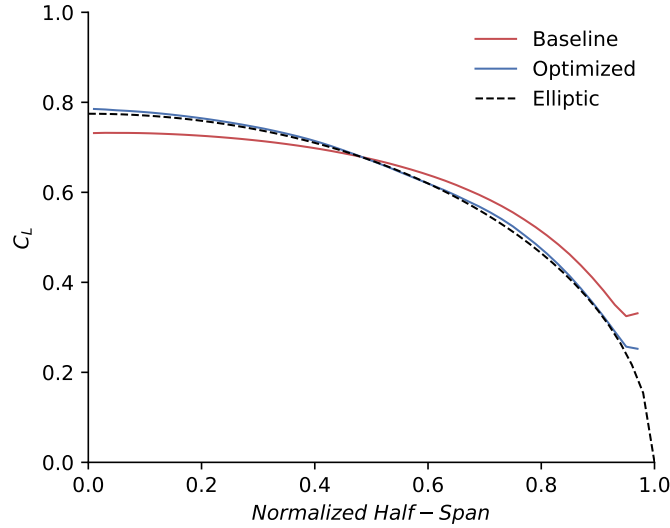


**Fig. 10 Change of  $C_L$  distribution along the span of the wing and theoretic elliptic lift distribution.**

impose curvature constraints to both streamwise and spanwise directions. However, for wing aerodynamic optimization, we need to impose the curvature constraints only in the spanwise direction. Therefore, we develop a new 1D curvature constraint that starts with defining multiple nodes lying on a straight line. These nodes are then projected on the design surface along the given direction, which is the  $y$  direction in this case. The projected point will be embedded into the FFD and move with the design surface; they will be snapped onto the design surface during optimization. Using the following equation (25), the curvature of the design surface at the projected point  $i$  is computed. Note that we take a square of the curvature to make sure it is always positive. We then take the average of the squared-curvature for all projected points and use it as the constraint value. The above curvature constraint has been implemented in pyGeo.

$$C_i^2 = \left( \frac{y_{i+1} - 2y_i + y_{i-1}}{\varepsilon^2} \right)^2 \quad (25)$$

The optimization ran for 260 iterations. The variation of the  $C_D$  and optimality can be seen on Fig. 7. In the first few iterations,  $C_D$  is higher than the baseline geometry because of the penalty parameter.

As the result of optimization, the drag decreased by 11.4%, where the optimality of this result is 3.3E-04 and the

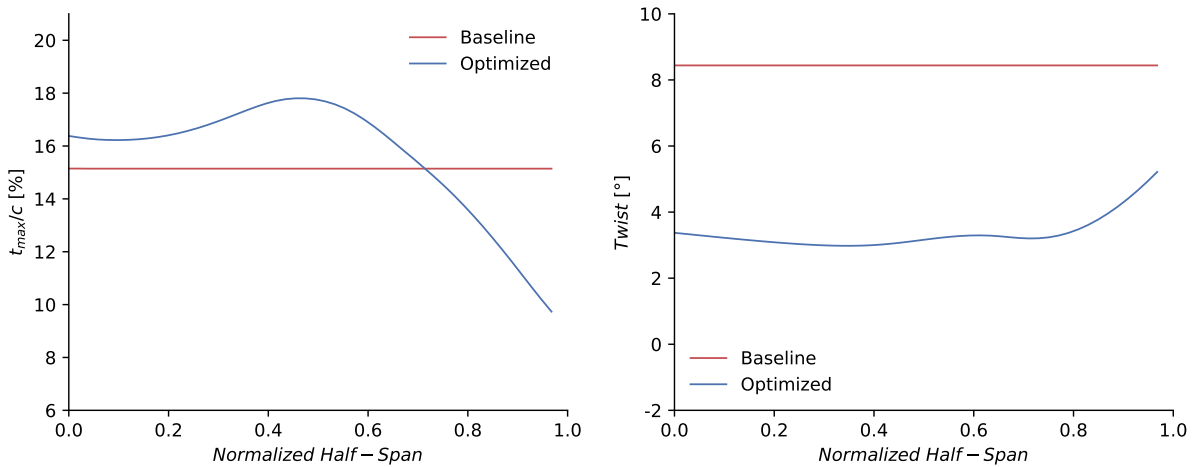


**Fig. 11 Change of geometric parameters of the wing along the span. Left: thickness. Right: twist.**

**Table 7 Formulation of optimization problems with single propeller.** The design variable with a superscript are common for all six optimizations. The design variable with superscripts are specific to these optimizations. (a:Wing\_Propeller\_Fixed, b:Wing\_Propeller\_x, c:Wing\_Propeller\_y, d:Wing\_Propeller\_z, e:Wing\_Propeller\_xyz, f:Wing\_Propeller\_xy<sub>r2</sub>)

	Function/Variable	Description	Quantity
Minimize	$C_D$	Drag coefficient of the wing	
with respect to	$-10 \leq \gamma \leq 10$	Twist of each FFD section	6
	$-1.0 \leq \Delta y \leq 1.0$	Vertical displacements of FFD points	120
	$-0.15 \leq x_p \leq -0.15$	Longitudinal position of propeller center	$1^{b,e,f}$
	$-0.05 \leq y_p \leq 0.05$	Vertical position of propeller center	$1^{c,e,f}$
	$0.1 \leq z_p \leq 0.6$	Lateral position of propeller center	$1^{d,e,f}$
	$0.09 \leq r_2 \leq 0.15$	Propeller outer radius	$1^f$
	<b>Total Design Variables</b>		<b>126<sup>a</sup>, 127<sup>b,c,d</sup>, 129<sup>e</sup>, 130<sup>f</sup></b>
subject to	$V_{bl} \leq V \leq 3 \cdot V_{bl}$	Minimum volume constraint	1
	$0.5 \cdot t_{bl} \leq t \leq 3 \cdot t_{bl}$	Minimum thickness constraint	240
	$\Delta y_{LE, upper} = \Delta y_{LE, lower}$	Fixed leading edge constraint	6
	$\Delta y_{TE, upper} = \Delta y_{TE, lower}$	Fixed trailing edge constraint	6
	$C_L = 0.6$	Lift constraint	1
	$r_{LE, bl} \leq r_{LE} \leq 3 \cdot r_{LE, bl}$	Leading edge radius constraint	1
	$0 \leq \kappa \leq 0.1$	Curvature constraints	4
	$z_p - r_2 > 0.05$	Actuator position constraint	1
	<b>Total Constraint Functions</b>		<b>260</b>

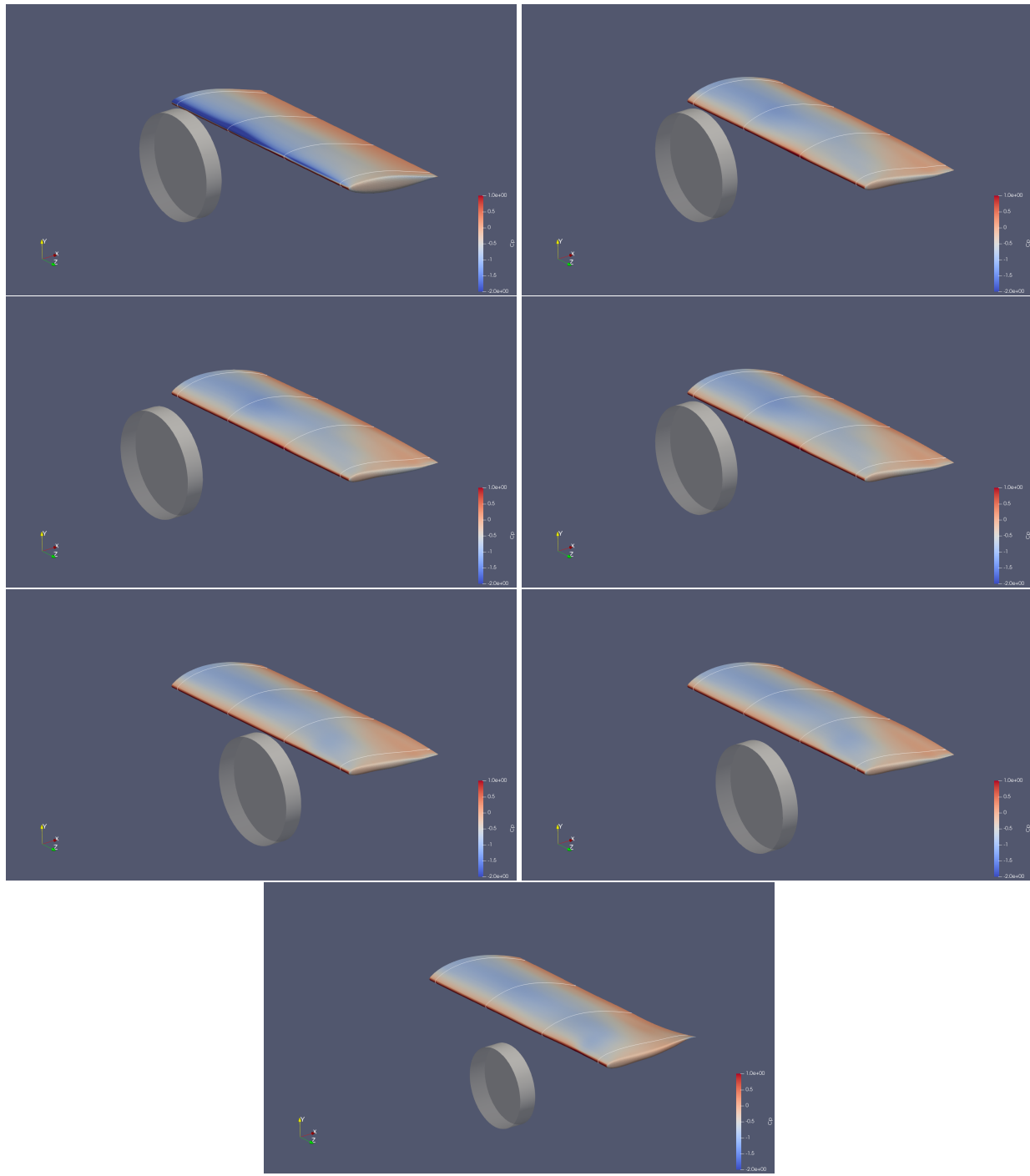
feasibility is 1.4E-08. The optimization results can be seen in Table 6, and the baseline and optimized wing geometries with 4 wing sections, which are used to investigate the change of  $C_P$  distribution can be seen on Fig.9.

Fig. 8 shows the selected wing sections to show the variation of  $C_P$  and change of airfoil. As can be seen, the symmetric airfoils are turned into cambered airfoils and the lift produced by the rear of the wing is increased. The change of lift distribution can be seen on Fig. 10, the optimized lift distribution on wing is aligned with the theoretical elliptical distribution.

The baseline geometry has the same thickness and twist along its span, however both of them are variable on the optimized geometry. The thickness at the root and middle of the wing is thicker, and the thickness at the tip of the wing is thinner on the optimized geometry. Even the optimized twist is higher at the tip than root and middle of the wing, it is

**Table 8 Summary of results for optimizations with single propeller. "dv" subscript indicates effect of design variables which are used in this case but not used in Wing\_Propeller\_Fixed. The  $C_D=0.04149$  for the baseline geometry. The actuator parameters which are used as design variables are underlined.**

Optimization	$C_D$	% $\Delta C_D$	% $\Delta C_{D_{dv}}$	$x_p$	$y_p$	$z_p$	$r_2$
Wing_Propeller_Fixed	0.03662	-11.742	-	-0.2	0.0	0.3	0.12
Wing_Propeller_x	0.03644	-12.183	-0.441	<u>-0.25</u>	0.0	0.3	0.12
Wing_Propeller_y	0.03662	-11.743	-0.002	-0.2	<u>-0.00134</u>	0.3	0.12
Wing_Propeller_z	0.03256	-21.533	-9.971	-0.2	0.0	<u>0.58363</u>	0.12
Wing_Propeller_xyz	0.03247	-21.761	-10.019	<u>-0.25</u>	<u>-0.00514</u>	<u>0.58197</u>	0.12
Wing_Propeller_xy <sub>r2</sub>	0.03189	-23.135	-11.394	<u>-0.25</u>	<u>0.00819</u>	<u>0.59557</u>	0.09



**Fig. 12** Baseline geometry ( $1^{st}$  row, left), Wing\_Propeller\_Fixed geometry ( $1^{st}$  row, right), Wing\_Propeller\_x geometry ( $2^{nd}$  row, left), Wing\_Propeller\_y geometry ( $2^{nd}$  row, right), Wing\_Propeller\_z geometry ( $3^{rd}$  row, left), Wing\_Propeller\_xyz geometry ( $3^{rd}$  row, right), Wing\_Propeller\_xyzt geometry ( $4^{th}$  row). Also 4 wing sections used to show the change of  $C_P$  distribution are visible.

still less than the baseline geometry along the span. Both thickness and twist changes can be seen of Fig. 11.

#### D. Coupled wing-propeller aerodynamic optimizations (single propeller)

In this section, results for coupled aerodynamic shape and propeller parameters optimization are demonstrated. The propeller parameters are restricted as the lateral, longitudinal and vertical positions and the outer radius of the propeller blade. This group of optimizations are done by adding a single propeller to Wing\_Only setup. The purpose of these optimizations is to investigate which actuator parameter is the most effective to decrease the drag. The list of these optimizations can be seen in Table 7. The objective function is the drag coefficient ( $C_D$ ) and nominal flight condition is at lift coefficient ( $C_L$ ) of 0.6 like Wing\_Only. The common design variables for each optimization are the twist angle ( $\gamma$ ) and the 120 FFD points moving in the vertical (y) direction. The additional design variables are longitudinal ( $x_p$ ) position of propeller center for Wing\_Propeller\_x, vertical ( $y_p$ ) position of propeller center for Wing\_Propeller\_y, lateral ( $z_p$ ) position of propeller center for Wing\_Propeller\_z, 3D ( $x_p, y_p, z_p$ ) position of propeller center for Wing\_Propeller\_xyz, and 3D ( $x_p, y_p, z_p$ ) position of propeller center and outer radius ( $r_2$ ) of the propeller for Wing\_Propeller\_xy $r_2$ . The constraint functions are the same functions with the Wing\_Only case and additional actuator position constraint, which prevents the movement of the actuator's center into the symmetry plane. The wing geometry and the flow conditions are the same with the Wing\_Only case. Inner radius of actuator is 0.035 m and outer radius is 0.12 m. The total axial force is fixed as 55N for optimizations with propeller.

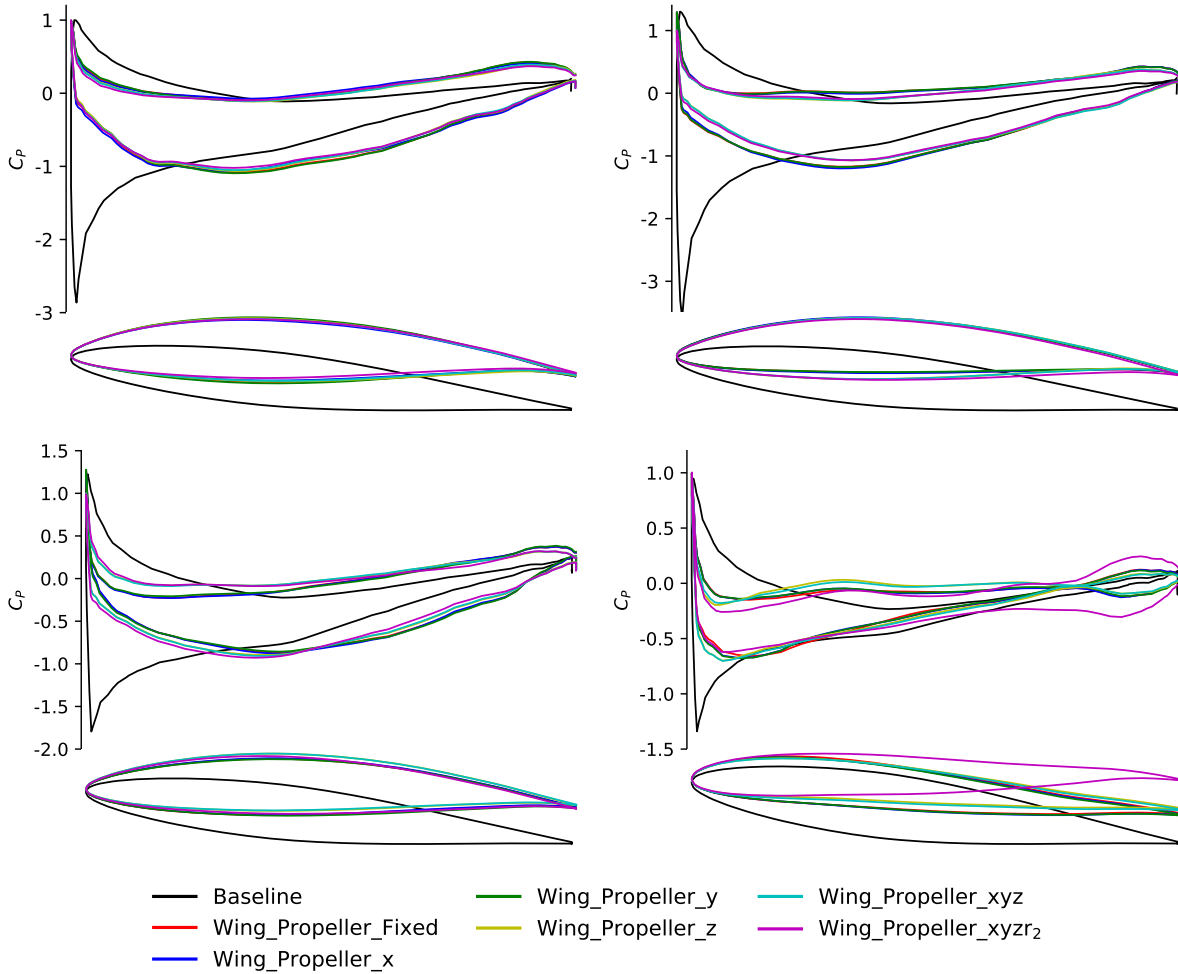


**Fig. 13** Change of  $C_P$  distribution and airfoil shape at different wing sections. Top left: 3% span. Top right: 31% span. Bottom left: 63% span. Bottom right: 94% span. Black color denotes baseline geometry, red color denotes Wing\_Propeller\_Fixed geometry, blue color denotes Wing\_Propeller\_x geometry, green color denotes Wing\_Propeller\_y geometry, yellow color denotes Wing\_Propeller\_z geometry, cyan color denotes Wing\_Propeller\_xy geometry, and magenta color denotes Wing\_Propeller\_xy $r_2$  geometry

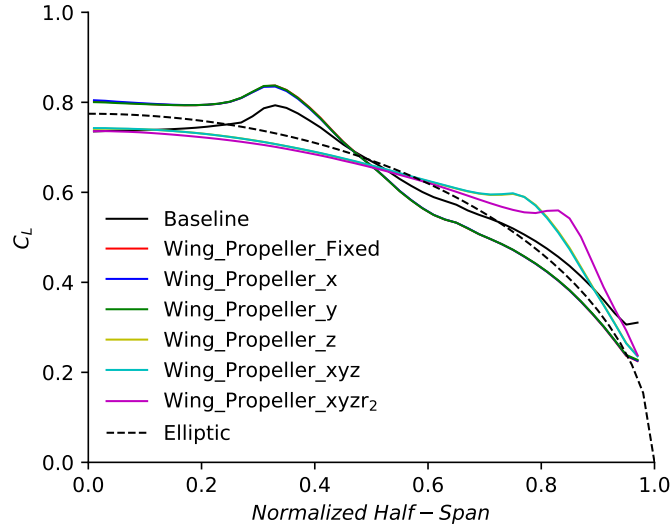


**Fig. 14 Change of  $C_L$  distribution along the span of the wing**

Table 8 summarizes the optimization results for all the six cases mentioned above. The largest drag reduction (22.86%) is achieved by allowing the propeller to move in all the three directions, as well as changing its outer radius. The most important design variable is the lateral ( $z_p$ ) position of the propeller center. The effects of longitudinal ( $x_p$ ) and vertical ( $y_p$ ) position of the propeller center are less than 5% and 0.02% of lateral ( $z_p$ ) position respectively, and their total effect is even smaller than sum of their individual effects. The second most important parameter is the outer radius ( $r_2$ ) of the propeller, whose effect is 10% of lateral ( $z_p$ ) position of the propeller. The change of the propeller design variables in these optimizations can be seen on Fig.12. When  $z_p$  is allowed to move, the optimizer always moves the propeller to the tip of the wing to reduce the intensity of the tip vortex to reduce the induced drag, as expected. The movement in the  $y_p$  direction is small, indicating that the impact of the propeller  $y$  location on the drag is small. The movement in the  $x_p$  axis is away from the wing. The  $r_2$  decreased in the last optimization case. We speculate this is because reducing the outer radius increases the axial and tangential force per area (the total thrust is fixed at 55 N). Therefore, the tangential component of the propeller wake becomes stronger to further reduce the wing tip vortex. Note that all design variables except for  $x_p$  reach their bounds.

Figure 13 shows the same wing spanwise sections as the Wing\_Only to show the variation of  $C_P$  and change of wing

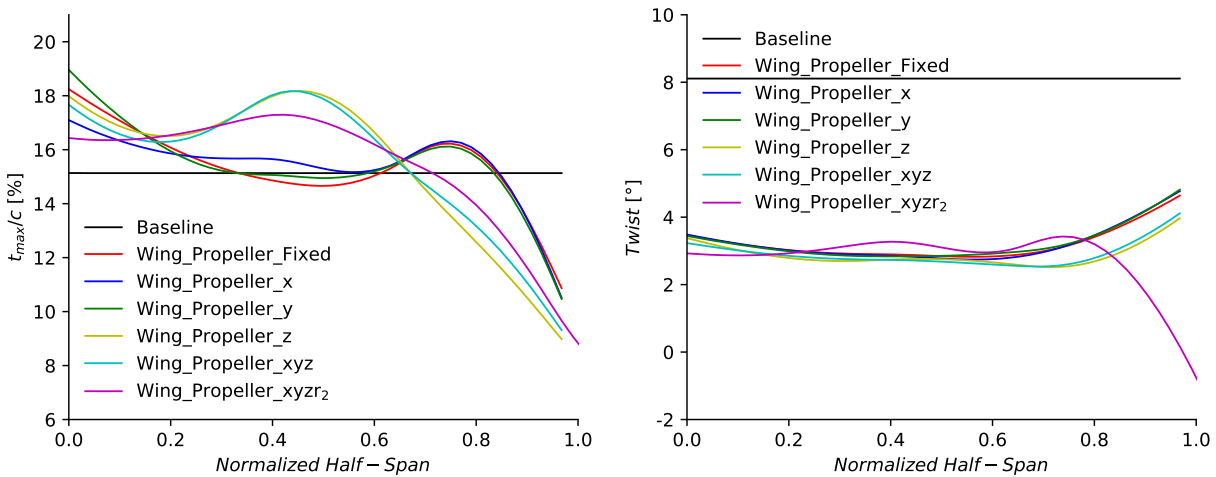


**Fig. 15 Change of geometric parameters of the wing along the span. Left: thickness. Right: twist.**

**Table 9 Formulation of optimization problems with single propeller. The design variable with a superscript are common for all six optimizations. The design variable with superscripts are specific to these optimizations. (a:Wing\_2Propellers\_Fixed, b:Wing\_2Propellers\_xydr<sub>2</sub>)**

	Function/Variable	Description	Quantity
Minimize	$C_D$	Drag coefficient of the wing	
with respect to	$-10 \leq \gamma \leq 10$ $-1.0 \leq \Delta y \leq 1.0$ $0.1 \leq z_{p,inner} \leq 0.4$ $0.3 \leq z_{p,outer} \leq 0.6$ $0.05 \leq r_2 \leq 0.09$	Twist of each FFD section Vertical displacements of FFD points Lateral position of propeller center Lateral position of propeller center Propeller outer radius	6 120 1 <sup>a</sup> 1 <sup>a</sup> 1 <sup>a</sup>
		<b>Total Design Variables</b>	<b>126<sup>a</sup>, 129<sup>b</sup></b>
subject to	$V_{bl} \leq V \leq 3 \cdot V_{bl}$ $0.5 \cdot t_{bl} \leq t \leq 3 \cdot t_{bl}$ $\Delta y_{LE, upper} = \Delta y_{LE, lower}$ $\Delta y_{TE, upper} = \Delta y_{TE, lower}$ $C_L = 0.6$ $r_{LE, bl} \leq r_{LE} \leq 3 \cdot r_{LE, bl}$ $0 \leq \kappa \leq 0.1$ $z_{p,inner} - r_{2,inner} > 0.05$ $r_{2,inner} = r_{2,outer}$ $z_{tip,outer} - z_{tip,inner} > 0.05$	Minimum volume constraint Minimum thickness constraint Fixed leading edge constraint Fixed trailing edge constraint Lift constraint Leading edge radius constraint Curvature constraints Actuator position constraint Actuator radius equality constraint Actuator distance constraint	1 240 6 6 1 1 4 1 1 1 1
		<b>Total Constraint Functions</b>	<b>261<sup>a</sup>, 262<sup>b</sup></b>

shape. The pressure distributions have the same trend for all optimizations except for the tip. The variation of  $C_P$  at the tip of Wing\_Propeller\_xydr<sub>2</sub> case is different than others, the difference between  $C_P$  at the top and bottom surfaces is more homogeneously distributed along the span and there is huge difference between them the tip. The symmetric airfoils are turned into cambered airfoils and the lift produced by the rear of the wing is increased like Wing\_Only case. The change of lift distribution can be seen on Fig. 14. The optimized lift distributions on wing are not aligned with the theoretical elliptical distribution because of the effect of the propeller, as was also mentioned by Kroo [11].

Figure 15 shows the maximal thickness and twist distribution along the span. Generally, the maximal thickness at the root and middle of the wing is thicker, and the thickness at the tip of the wing is thinner on the optimized geometries like Wing\_Only case. The position of the propeller has a higher impact on the thickness distribution than the twist distribution. Various optimization cases exhibit a large variation in the maximal thickness distribution in the spanwise direction. In contrast, twist distribution shows relatively small variation and it is similar for each optimization cases except the Wing\_Propeller\_xydr<sub>2</sub> case, the twist of it differs than the others especially at the outermost quarter of the wing span, where decreases even below 0°. Apart from Wing\_Propeller\_xydr<sub>2</sub>, general trend of twist distribution of all others are similar with Wing\_Only case.

#### E. Coupled wing-propeller aerodynamic optimizations (double propellers)

In this subsection, the coupled wing-propeller aerodynamic optimization with two propellers are demonstrated. The propeller parameters are restricted as the lateral position and the outer radius of the propeller. This optimization group is created by adding two propellers to the Wing\_Only setup. Unlike optimizations with single propeller, the radius and the lateral locations of the centers of these propellers are not the same with the "Validation" baseline geometry. The outer radii of the both propellers are set to 0.07, and their lateral locations are  $z_{p,inner}=0.25$  and  $z_{p,outer}=0.45$  in the baseline setup. The total axial force is fixed as 55 N for the optimizations; each propeller generates 27.5 N thrust. The most effective design variables of propeller are found as  $z_p$  and  $r_2$  from the above optimizations. Therefore,

**Table 10** Summary of results for optimizations with single propeller. "dv" subscript indicates effect of design variables which are used in this case but not used in Wing\_2Propellers\_Fixed. The  $C_D=0.04196$  for the baseline geometry.

Optimization	$C_D$	% $\Delta C_D$	% $\Delta C_{D_{dv}}$	$z_{p,inner}$	$z_{p,outer}$	$r_2$
Wing_2Propellers_Fixed	0.03690	-12.072	-	0.25	0.45	0.07
Wing_2Propellers_zr2	0.03331	-20.634	-8.563	<u>0.4315</u>	<u>0.6</u>	<u>0.05926</u>

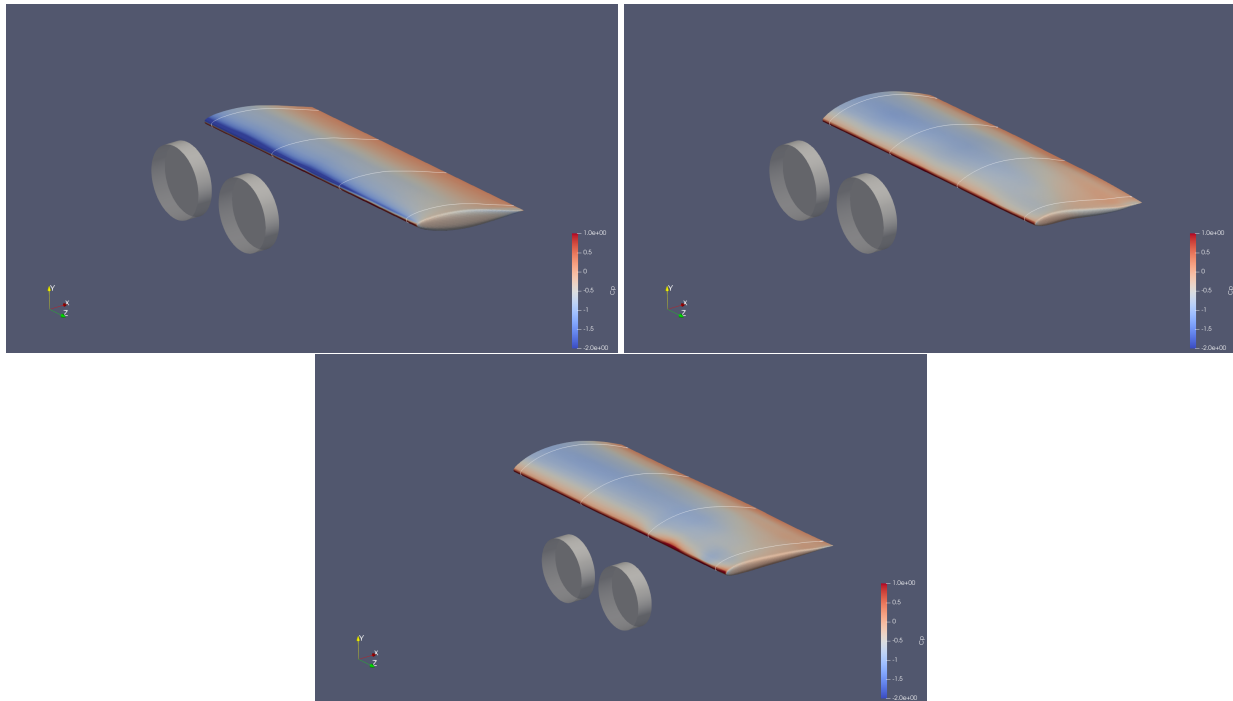


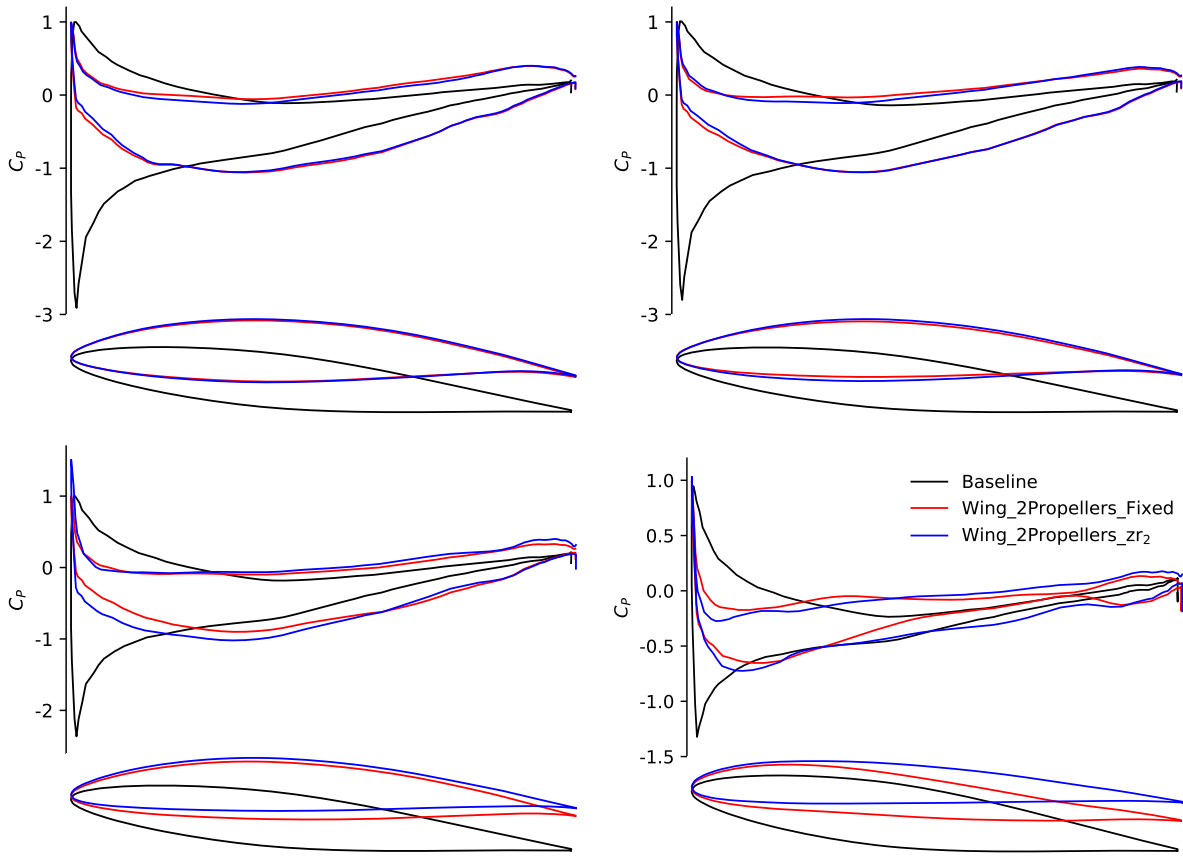
**Fig. 16** Baseline geometry (left), Wing\_2Propellers\_Fixed geometry (middle), Wing\_2Propellers\_zr2 geometry (right). Also 4 wing sections used to show the change of  $C_P$  distribution are visible.

the optimization for two propeller case are done only for a setup with fixed propellers and a setup with the addition of these two design variables. The formulation of these optimizations is shown in Table 9, the objective function is the drag coefficient ( $C_D$ ) and nominal flight condition is at lift coefficient ( $C_L$ ) of 0.6 like the previous optimizations. The common design variables for each optimization are the twist angle ( $\gamma$ ), 120 FFD points moving in the vertical (y) direction, and the additional design variables are  $z_p$  and  $r_2$  for the Wing\_2Propellers\_xy $z_2$ . The constraint functions are the same functions as the single propeller optimizations. There is one additional actuator radius equality constraints, which link the radius of both propellers. In other words, the two propellers must have the same outer radius. In addition, we impose a propeller-distance constraint to prevent the propellers from overlap with each other.

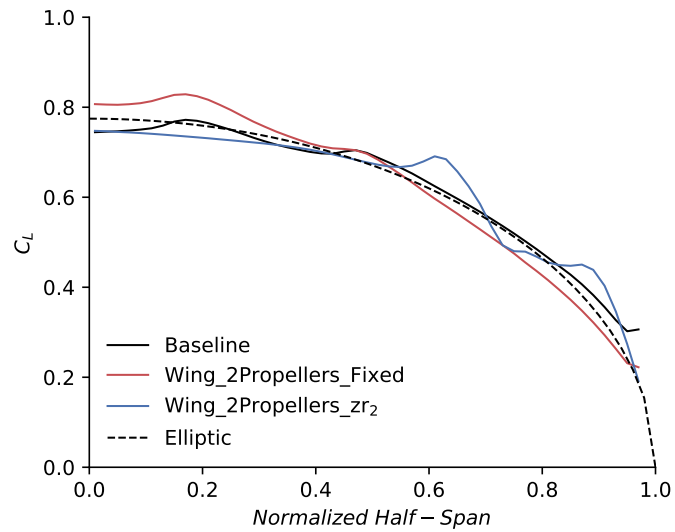
As shown in Table 10, the effect of design variables  $z_p$  and  $r_2$  are similar with the optimizations of single propeller setup. The change of the propeller design variables in these optimizations can be seen in Fig.16. Both propellers move to the tip of wing, and the  $r_2$  decreased in Wing\_2Propellers\_xy $z_2$  similar with Wing\_Propeller\_xy $z_2$ . Even though  $z_p$  variables are equal to their upper boundaries, the  $r_2$  value are not equal to one of its boundaries for the optimized design.

Figure 17 shows the same wing spanwise sections as the previous optimizations to show the variation of  $C_P$  and change of wing shape. The pressure distributions have the same trend except for the tip. Here the  $C_P$  distribution is more uniform for Wing\_2Propellers\_xy $z_2$  than Wing\_2Propellers\_Fixed. The symmetric airfoils are turned into cambered airfoils and the lift produced by the rear of the wing is increased like the previous optimization cases. The change of lift distribution is shown in Fig. 18. The optimized lift distributions on wing are not aligned with the theoretical elliptical distribution because of the effect of the propeller.

The maximal thickness and twist distribution for the baseline and optimized cases are shown in Fig. 19. Generally,



**Fig. 17** Change of  $C_p$  distribution and airfoil shape at different wing sections. Top left: 3% span. Top right: 31% span. Bottom left: 63% span. Bottom right: 94% span. Black color denotes baseline geometry, red color denotes Wing\_2Propellers\_Fixed geometry, blue color denotes Wing\_2Propellers\_zr2 geometry



**Fig. 18** Change of  $C_L$  distribution along the span of the wing

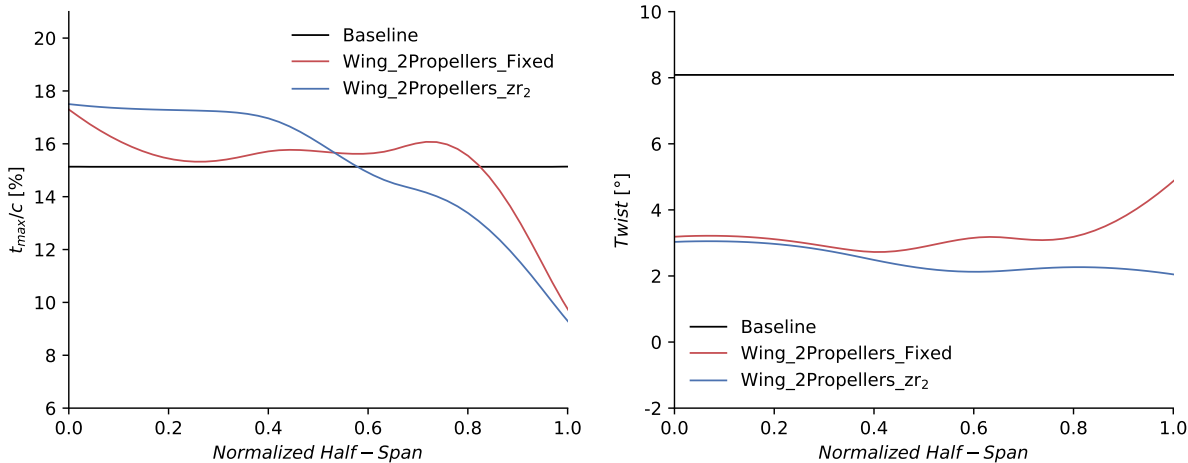


**Fig. 19** Change of geometric parameters of the wing along the span. Left: thickness. Right: twist.

the maximal thickness at the root and middle of the wing is thicker, and the thickness at the tip of the wing is thinner on the optimized geometries like the previous optimizations cases. The maximal thickness of Wing\_2Propellers\_Fixed steeply decreases at the root and does not exhibit high variation between 20% and 80% of the span, and then decreases steeply again. However, the maximal thickness of Wing\_2Propellers\_xyzt2 is nearly flat at first 40% of the span then starts to decrease. The twist distribution shows higher variation in Wing\_2Propellers\_Fixed case than Wing\_2Propellers\_xyzt2, and unlike other cases, twist distribution at the tip of the wing is less than the root in the Wing\_2Propellers\_xyzt2 case.

#### IV. Conclusion

In this study, we developed a simultaneous wing and propeller optimization capability by using the adjoint method. A rectangular wing is used as the baseline design and propellers are modeled as actuator disks. We used a smoothed actuator force distribution to allow changing propeller parameters along with the wing shape during the optimization. The flow condition of optimizations is at 0.3 Mach, 0.6 lift coefficient, and  $2.2 \times 10^5$  Reynolds number.

The optimization results show that simultaneous optimization of the wing and propeller increases drag reduction up to 11.1 % compared with optimizing only the wing with a fixed propeller. The location of the propeller center and the outer radius of propeller are used as design variables. The center of optimized propeller moves away from the wing on longitudinal direction, moves to the tip of the wing in lateral direction and moves in vertical direction negligibly, and the radius of optimized propeller reduces. The lateral position of the center and the outer radius of the propeller are the most effective design variables, whose combined effect contributes more than 95% of all drag reduction. Pressure and lift distributions of simultaneously optimized and only wing optimized geometries show similar trends. The total drag reduction is increased with increasing number of propeller design variables, as expected.

This study showed that simultaneous optimization of wing and propeller has benefit compared with optimizing them separately. This study serves as the starting point for more detailed high-fidelity wing-propeller aerodynamic optimizations.

#### Acknowledgments

The authors thank the Hyundai Motor Company for funding this research.

#### References

- [1] Patterson, M. D., Daskilewicz, M. J., , and German, B., "Conceptual Design of Electric Aircraft with Distributed Propellers: Multidisciplinary Analysis Needs and Aerodynamic Modeling Development," *52nd Aerospace Sciences Meeting*, AIAA Paper 2014-0534, 2014. <https://doi.org/10.2514/6.2014-0534>.
- [2] Moore, M. D., , and Fredericks, B., "Misconceptions of Electric Aircraft and their Emerging Aviation Markets," AIAA Paper 2014-0535, 2014.

- [3] Stoll, A. M., Bevirt, J. B., Moore, F., M. D., J., W., and Borer, N. K., "Drag Reduction Through Distributed Electric Propulsion," *14th AIAA Aviation Technology, Integration, and Operations Conference*, AIAA Paper 2014-2851, 2014. <https://doi.org/10.2514/6.2014-2851>.
- [4] Hwang, J. T., and Ning, A., "Large-Scale Multidisciplinary Optimization of an Electric Aircraft for On-Demand Mobility," *2018 AIAA/ASCE/AHS/ASC Structures, Structural Dynamics, and Materials Conference*, AIAA Paper 2018-1384, 2018. <https://doi.org/10.2514/6.2018-1384>.
- [5] Brelje, B. J., and Martins, J. R. R. A., "Electric, Hybrid, and Turboelectric Fixed-Wing Aircraft: A Review of Concepts, Models, and Design Approaches," *Progress in Aerospace Sciences*, Vol. 104, Jan 2019, pp. 1–19. <https://doi.org/10.1016/j.paerosci.2018.06.004>.
- [6] Moore, K. R., and Ning, A., "Takeoff and Performance Trade-Offs of Retrofit Distributed Electric Propulsion for Urban Transport," *Journal of Aircraft*, Vol. 56, No. 5, 2019, pp. 1880–1892. <https://doi.org/10.2514/1.c035321>.
- [7] de Vries, R., Hoogreef, M., and Vos, R., "Preliminary Sizing of a Hybrid-Electric Passenger Aircraft Featuring Over-the-Wing Distributed-Propulsion," *Journal of Aircraft*, Vol. 57, No. 1, 2020, pp. 93–112. <https://doi.org/10.2514/6.2019-1811>.
- [8] Veldhuis, L. L. M., and Heyma, P. M., "Aerodynamic Optimisation of Wings in Multi-Engined Tractor Propeller Arrangements," *Aircraft Design*, Vol. 3, No. 3, 2000, pp. 129–149. [https://doi.org/10.1016/s1369-8869\(00\)00010-0](https://doi.org/10.1016/s1369-8869(00)00010-0).
- [9] Rakshith, B. R., Deshpande, S. M., Narasimha, R., and Praveen, C., "Optimal Low-Drag Wing Planforms for Tractor-Configuration Propeller-Driven Aircraft," *Journal of Aircraft*, Vol. 52, No. 6, 2015, pp. 1791–1801.
- [10] Deere, K. A., Viken, J. K., Viken, S., Carter, M. B., Wiese, M., and Farr, N., "Computational Analysis of a Wing Designed for the X-57 Distributed Electric Propulsion Aircraft," *35th AIAA Applied Aerodynamics Conference*, AIAA Paper 2017-3923, 2017. <https://doi.org/10.2514/6.2017-3923>.
- [11] Kroo, I., "Propeller–Wing Integration for Minimum Induced Loss," *Journal of Aircraft*, Vol. 23, 1986, pp. 561–565. <https://doi.org/10.2514/3.45344>.
- [12] Witkowski, D. P., Lee, A. K. H., and Sullivan, J. P., "Aerodynamic Interaction Between Propellers and Wings," *Journal of Aircraft*, Vol. 26, 1989, pp. 829–836. <https://doi.org/10.2514/3.45848>.
- [13] Gomariz-Sancha, A., Maina, M., and Peace, A. J., "Analysis of Propeller-Airframe Interaction Effects Through a Combined Numerical Simulation and Wind-Tunnel Testing Approach," *53rd AIAA Aerospace Sciences Meeting*, AIAA Paper 2015-1026, 2015. <https://doi.org/10.2514/6.2015-1026>.
- [14] Stokkermans, T. C. A., van Arnhem, N., Sinnige, T., and Veldhuis, L. L. M., "Validation and Comparison of RANS Propeller Modeling Methods for Tip-Mounted Applications," *AIAA Journal*, Vol. 57, 2019, pp. 566–580. <https://doi.org/10.2514/1.J057398>.
- [15] Alba, C., Elham, A., German, B. J., , and Veldhuis, L. L. M., "A Surrogate-Based Multi-Disciplinary Design Optimization Framework Modeling Wing–Propeller Interaction," *Aerospace Science and Technology*, Vol. 78, July 2018, pp. 721–733. <https://doi.org/10.1016/j.ast.2018.05.002>.
- [16] Stokkermans, T., Veldhuis, L., Soemarwoto, B., Fukari, R., and Eglin, P., "Aerodynamic Interaction Between Propellers and Wings," *Aerospace Science and Technology*, Vol. 101, June 2020, pp. 829–836. <https://doi.org/10.1016/j.ast.2020.105845>.
- [17] Chauhan, S. S., and Martins, J. R. R. A., "RANS-Based Aerodynamic Shape Optimization of a Wing Considering Propeller–Wing Interaction," *Journal of Aircraft*, Vol. 58, June 2021, pp. 497–513. <https://doi.org/10.2514/1.C035991>.
- [18] Spalart, P., , and Allmaras, S., "A One-Equation Turbulence Model for Aerodynamic Flows," *30th Aerospace Sciences Meeting and Exhibit*, AIAA Paper 1992-439, 1992. <https://doi.org/10.2514/6.1992-439>.
- [19] Patankar, S. V., and Spalding, D. B., "A calculation procedure for heat, mass and momentum transfer in three-dimensional parabolic flows," *International Journal of Heat and Mass Transfer*, Vol. 15, No. 10, 1972, pp. 1787–1806.
- [20] Rhee, C., and Chow, W. L., "Numerical study of the turbulent flow past an airfoil with trailing edge separation," *AIAA Journal*, Vol. 21, No. 11, 1983, pp. 1525–1532. <https://doi.org/10.2514/3.8284>.
- [21] He, P., Mader, C. A., Martins, J. R. R. A., and Maki, K. J., "An Aerodynamic Design Optimization Framework Using a Discrete Adjoint Approach with OpenFOAM," *Computers & Fluids*, Vol. 168, 2018, pp. 285–303. <https://doi.org/10.1016/j.compfluid.2018.04.012>.

- [22] He, P., Mader, C. A., Martins, J. R. R. A., and Maki, K. J., “DAFoam: An Open-Source Adjoint Framework for Multidisciplinary Design Optimization with OpenFOAM,” *AIAA Journal*, 2020. <https://doi.org/10.2514/1.J058853>.
- [23] Kenway, G. K. W., Mader, C. A., He, P., and MArtins, J. R. R. A., “Effective adjoint approaches for computational fluid dynamics,” *Progress in Aerospace Sciences*, Vol. 110, 2019, p. 100542. <https://doi.org/10.1016/j.paerosci.2019.05.002>.
- [24] Balay, S., Abhyankar, S., Adams, M. F., Brown, J., Brune, P., Buschelman, K., Dalcin, L., Dener, A., Eijkhout, V., Gropp, W. D., Kaushik, D., Knepley, M. G., May, D. A., McInnes, L. C., Mills, R. T., Munson, T., Rupp, K., Sanan, P., Smith, B. F., Zampini, S., Zhang, H., and Zhang, H., “PETSc Users Manual,” *Tech. Rep. ANL-95/11 - Revision 3.10*, Argonne National Laboratory, 2018. <https://doi.org/10.2514/1.J058853>.
- [25] “Overview of MACH-Aero,” *MACH-Aero Documentation*, <https://mdolab-mach-aero.readthedocs-hosted.com/en/latest/machFramework/MACH-Aero.html>, 2021.
- [26] Wu, N., Kenway, G., Mader, C. A., Jasa, J., and Martins, J. R. R. A., “pyOptSparse: a Python framework for large-scale constrained nonlinear optimization of sparse systems,” *Journal of Open Source Software*, Vol. 5, No. 54, 2020, p. 2564. <https://doi.org/10.21105/joss.02564>, URL <https://doi.org/10.21105/joss.02564>.
- [27] Kenway, G., Kennedy, G., and Martins, J. R. R. A., *A CAD-Free Approach to High-Fidelity Aerostructural Optimization*, 2010. <https://doi.org/10.2514/6.2010-9231>.
- [28] Secco, N. R., Kenway, G. K., He, P., Mader, C., and Martins, J. R., “Efficient mesh generation and deformation for aerodynamic shape optimization,” *AIAA Journal*, Vol. 59, No. 4, 2021, pp. 1151–1168.
- [29] Veldhuis, L. L. M., “Propeller wing aerodynamic interference,” Ph.D. thesis, Technische Universiteit Delft, 2005.
- [30] “Nova,” *Nova | High Performance Computing*, <https://www.hpc.iastate.edu/guides/nova>, 2021.
- [31] Hoekstra, M., “A RANS-based analysis tool for ducted propeller systems in open water condition,” *International Shipbuilding Progress* 53, 2006, pp. 205–227.
- [32] He, P., and Martins, J. R. R. A., “A Hybrid Time-Spectral Approach for Aerodynamic Optimization with Unsteady Flow,” 2021. <https://doi.org/10.2514/6.2021-0278>.
- [33] He, P., Filip, G., Martins, J. R., and Maki, K. J., “Design optimization for self-propulsion of a bulk carrier hull using a discrete adjoint method,” *Computers & Fluids*, Vol. 192, 2019, p. 104259.